Development of a Pixelated Prompt Gamma Imaging Detector with $LaBr_3$–BGO in a Wedged Configuration

Jin-Long Wang,[1] Li-Wang Yang,[1,2,*] Xiao-Guang Wu,[1,†] Zi-Yang He,[1] Yun Zheng,[1] Cong-Bo Li,[1] Tian—Xiao Li,[1] Zi-Hao Zhao,[1] Ming Zheng,[1] Jin-Ze Li,[1] Yun-Qiu Li,[1] Rui Hong,[1] Jia-Nan Zou,[1] Shao-Xiong Guan,[1] and Jing Shi[1]

[1]*Department of Nuclear Physics, China Institute of Atomic Energy, Beijing 102413, China*
[2]*College of Science, Henan university of Technology, Zhengzhou 450001, China*

A new pixelated prompt gamma imaging detector (PPGID) was developed for prompt gamma spectrum and gamma source position measurement. The PPGID prototype is composed of 30 independent pixelated scintillator detectors that can simultaneously obtain the gamma spectrum. The prototype has two $LaBr_3$ scintillator modules for gamma ray spectrum measurement with good performance in terms of energy resolution and one BGO module with high efficiency in high-energy detection. Therefore, in this study, a compound advanced imaging device based on energy spectrum detection was designed, assembled, and tested with radioactive sources; This device is called a pixelated prompt gamma imaging detector system (PPGID). The PPGID can correctly measure the source position as predicted by the FOV mathematical model. Both $LaBr_3$ and BGO can reproduce the gamma spectrum of the radioactive source. The tested energy response of $LaBr_3$ is 0.03$\sim$2.6 MeV, and that of BGO is 1$\sim$2.6 MeV with ^{22}Na and ^{232}Th. Dedicated data acquisition software was developed for energy calibration and gamma count histogram distribution. The gamma count histogram can be transformed into a thermal map which is the basis of the image.

Keywords: PPGID, FOV, SiPM, Scintillator, Gamma Spectrum

1. INTRODUCTION

The dosimetry advantages of proton therapy compared to conventional photon radiation therapy are caused by the Bragg peak[1]. However, the location of the Bragg peak inside the patient is sensitive to many factors, such as tissue density. Due to the steep dose gradient at the distal edge of the Bragg peak, uncertainties in the determination of this range can have a profound impact on the applied dose distribution[2–4]. Like proton therapy, carbon or helium therapy have the same range uncertainty problem[5–7]. Thus, new imaging modalities, such as in-beam PET[8–13], Compton cameras[14–18], proton CT[19, 20], prompt gamma imaging[21–31], and some other methods[32–34], have been developed to measure the range in vivo[35–37]. Different multi-slit prompt gamma cameras have been developed, such as knife-edge slits (KESs)[38] and multiparallel slits (MPSs)[39–41]. Examples include 12$\times$12 BGO scintillators with a crystal pixel size of 3.5$\times$3.5$\times$30 mm^3[25]and 2$\times$36 CsI(Tl) scintillators with a crystal pixel size of 3$\times$30$\times$100 mm^3[23]. These prototypes are designed for range assessment but this is not the only capability of prompt gamma. Proton–nuclear interactions involve both elastic and inelastic processes, including nuclear capture and nuclear scattering. For many scattering processes the tissue nuclei remain intact and are left in an excited energy state. The decay of these excited nuclei typically produces a gamma ray with an energy ranging from 0$\sim$11 MeV within a few nanoseconds of the proton–nucleus interaction. The energy spectra of this prompt gamma emission depend on the specific nuclear energy states of the excited elemental nuclei, resulting in each element producing a unique spectrum, known as prompt gamma spectroscopy. Thus, tissues composed of different elements and elemental concentrations will produce different emission spectra during irradiation. The characteristic energies and intensities of gamma rays can be used to determine the types of elements and their amounts [22, 42].

However, most (Prompt Gamma Image) PGI systems are not specifically developed for gamma spectroscopy measurements. For gamma spectrum investigation, Polf et al. characterized how prompt gamma (PG) emission from tissue changes as a function of carbon and oxygen concentrations[43, 44]. Paulo Martins et al. demonstrated a feasible technique for proton and ion beam spectroscopy (PIBS) that was capable of determining the elemental concentrations of irradiated tissues during particle therapy[21]. Based on these experiments. A prompt gamma spectrum retrieval algorithm (PGSRA) was developed by our group that could be used for element and density measurements for proton therapy[22]. A novel idear is to develop a new PGI system that can measure the proton range and simultaneously measure the element by a prompt gamma spectrum retrieval algorithm.

The challenge of PGSRA is to measure the spectrum along the proton beam path with small pixellated detector. The PPGID prototype is composed of 30 independent pixelated scintillator detectors that can simultaneously obtain the gamma spectrum along the beam path and in the vertical direction. $LaBr_3$ is the first candidate scintillator for gamma-ray spectrum measurements since it exhibits the best energy resolution, and BGO is the second candidate since it has high efficiency in high-energy detection[45]. Therefore, a compound advanced imaging device based on energy spectrum detection was designed, assembled, and tested by radioactivity in this study. This device is called the pixelated prompt gamma imaging detector system (PPGID). The expected performances of the PPGID in the prototype develop-

* Li-Wang Yang 446925336@qq.com
† Xiao-Guang Wu xingkong1973@sina.com

ment phase are: 1) measuring the gamma ray spectrum of different kinds of radioactive sources, 2) measuring the position of the sources in a high resolution.

2. REQUIREMENTS FOR PPGID

There are several basic requirements in designing the pixelated prompt gamma imaging detector system considering its future application in proton therapy[46].

1)The detector should be pixelated to obtain gamma rays along the beam path. To achieve longitudinal spatial resolution, only gammas perpendicular to the beam direction are allowed to enter the detector crystal. Thus, a collimator is needed.

2)The gamma-ray energy spectral response of the detector should be as wide as possible, and the energy resolution should be good. The ideal energy response range is 0.03∼8 MeV, and the resolution is approximately 6% at 511 keV.

3)To retrieve the tissue elements as needed by PGSRA, every pixel should independently measure the gamma spectrum. Thus, energy calibration should be performed before gamma detection or before data analysis.

4)Different energy windows can be set in the energy spectrum to facilitate the data analysis.

3. DESIGN OF THE PPGID

The design of the PPGID includes 4 aspects: 1) selection of the scintillator and photomultiplier; 2) specific front-end electronics design; 3) grating shielding (collimator) design and FOV mathematic model; and 4) data acquisition and software. The use of scintillators and photomultipliers is already discussed in our previous manuscript[45]. 2) and 3) are demonstrated in Sections 3.1-3.3. Data acquisition and software are introduced in Section 4.

3.1. Pixelated prompt gamma imaging detector

The pixelated prompt gamma imaging detector prototype has 3 modules, as shown in figure 1 a). The module 1 $LaBr_3$ ($5{\times}5{\times}50$ mm^3 with density 5.3 g/cm^3, 61000 photons/MeV), module 2 $LaBr_3$, and module 3 BGO ($5{\times}5{\times}50$ mm^3 with density 7.1 g/cm^3, 9000 photons/MeV) manufactured by Hebei Huakailong Technology Co., Ltd. Considering the decay time of the scintillators, the integration time of $LaBr_3$ is set as 640 ns and that of BGO is set as 1600 ns based on their event waveforms. More physical scintillator properties are discussed in our previous work[45].

Every module has 10 pixels with 1 cm pitch. The grey part is the grating shielding, which is made of tantalum. The square hole is 0.5 cm × 0.5 cm. The function of the grating shielding is to filter the photons such that only gamma rays parallel to the grating enter the scintillator. This feature ensures that every module from the PPGID can detect the distal edge location and thus measure the proton range. However, the pitch is 1 cm between the pixels in a module, and this parameter cannot be changed after manufacturing. This results in a very low resolution position measurements. Thus, the modules could be misaligned for high-resolution measurements, as shown in figure 1 b). The misalignment of two modules, three modules, and ten modules could increase the position resolutions to 0.5, 0.33, and 0.1 cm, respectively. The premise of this misalignment measurement method is that all modules should view the beam centre plane at the same time. Thus, wedges are used to form the angle between two modules, as shown in figure 1 c) and 1 d). The wedges are also made of tantalum and also functions as shield. The angle θ is formed between the modules to satisfy Equation 6 to ensure that the pixels from different modules view the same central position which will be discussed in section 3.3.3.

An expanded view of a single module from the PPGID is shown in figure 2. Gamma photons are filtered through a tantalum multiparallel grating (with a length of 8 cm, lateral thickness of 0.5 cm, and a hole in the center of 0.5 cm × 0.5 cm). In our previous investigation Figure 7 of reference [22] shows the 9 MeV gamma range in tantalum. 70% gammas are stopped after 2 cm and 90% gammas are stopped after 5 cm. Thus, the length of the tantalum grating can be 5 cm. While this manuscript 8 cm is adopted[25]. Then, gamma rays enter the scintillator, which generates visible light. The light is converted into an electrical signal by the SiPM on the front-end electronics, including the SiPM board, transfer board and amplifier board. To prevent the entry of ambient light, the scintillators and their junction to the grating shielding and SiPMs are tightly covered with black masks.

Knife-edge slits (KESs) and multiparallel slits (MPSs) are widely used for range assessment [39, 47, 48]. The overall balance of these two deviations from conditions of equal performance is a better detection efficiency for the KES and a better spatial resolution for the MPS one[40]. The misalignment of three multiparallel grating silits in the PPGID could increase the position resolution.

3.2. Front-End Electronics

Specific front-end electronics for every independent pixel are developed for the PPGID system, as shown in diagram figure 3. When the scintillator detects the gamma ray, it generates visible light, which is converted into an electrical signal by the SiPM (MicroFJ-60035-TSV) manufactured by SensL. The original SiPM signal is amplified by the forwards amplifier circuit and then output to the back-end data acquisition system. There are 3 boards: the SiPM, transfer and amplifier boards, as shown in figure 2. 10 SiPMs are stacked in the parallel form of a $1{\times}10$ array. This design has four advantages : 1) it can easily dissipate heat, 2) it has a modular design for different kinds of scintillators, 3) misalignment is easily achieved along the beam direction to increase the position resolution for future range measurement, and 4) the wedge angle can be easily changed for vertical measurement.

The first SiPM board is the $1{\times}10$ SiPM array. The chip size is $6{\times}6$ mm^2, and the pitch is 10 mm, as shown in figure

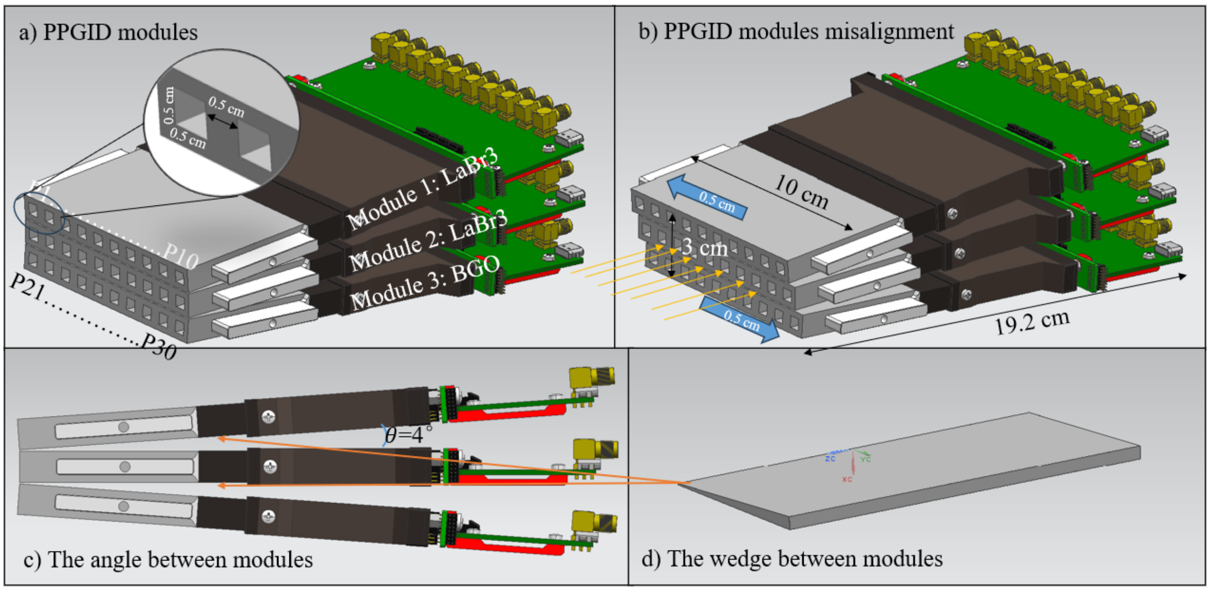

Fig. 1. Pixelated prompt gamma imaging detector modules, a) shows the detector has 3 modules, Module 1 LaBr3, Module2 LaBr3, and Module3 BGO. every module has 10 pixels and each pixel has a 0.5 cm × 0.5 cm collimator. b) shows the PPGID modules could be misaligned for high-resolution measurements. c) and d) shows the wedges are used to form the angle between two modules.

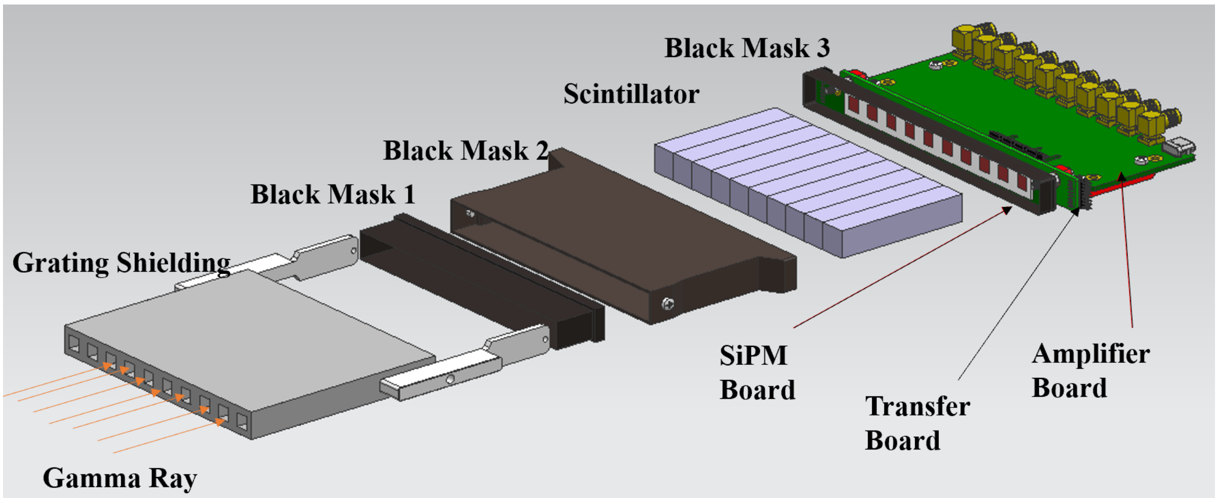

Fig. 2. Expanded view of a single module from the PPGID. Gamma photons are filtered through a tantalum multiparallel grating (collimator in gray), and a hole in the centre. Gamma rays enter the scintillator (in silver), which generates visible light. The light is converted into an electrical signal by the SiPM board (in green), transfer board, and amplifier board. To prevent the entry of ambient light, the scintillators and their junction to the grating shielding and SiPMs are tightly covered with black masks.

2. The signals from each SiPM are independently sent to the amplifier. This is the basis of PPGID, as every pixel functions as an eye to view a small region along the beam path.

The second is the transfer board, which connects the SiPM board and the amplifier board. The third is an amplifier board composed of a front amplifier, SiPM bias voltage/temperature compensation circuit, digital potentiometer, voltage conversion circuit, and microprogrammed control unit (MCU), as shown in figure 4. The MCU controls the compensator in real time to adjust the temperature on the SiPM while heat is generated when the transfer board is powered on. It also controls the digital potentiometer to adjust the gain of the front amplifier. SiPMs are temperature-sensitive devices. Thus, a temperature measurement chip is arranged on the back side of the SiPM array board to monitor the ambient temperature. The temperature data are transmitted to a temperature compensation circuit, which adjusts the bias voltage of the SiPM power supply based on the breakdown voltage change rate of approximately 21.5 mV/°C.

The third board is also a power supply board composed of a USB connector. There are 10 subminiature version A connectors (SMAs) to output 10 amplified signals to the data

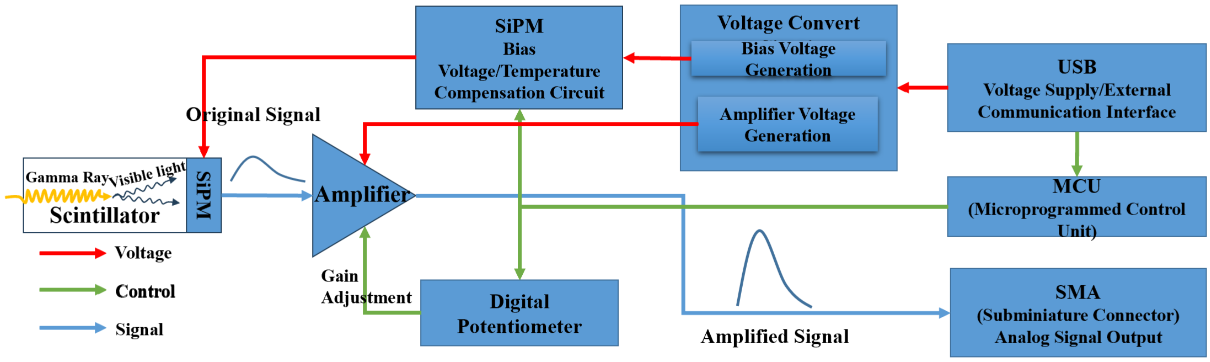

Fig. 3. Diagram of the front-end electronics for one pixel. When the scintillator detects the gamma ray, it generates visible light, which is converted into an electrical signal by the SiPM. The original SiPM signal is amplified by the forwards amplifier circuit and then output to the back-end data acquisition system. The red arrow indicates the power supply, the green line indicates the control flow, and the blue arrow indicates the signal transmission direction.

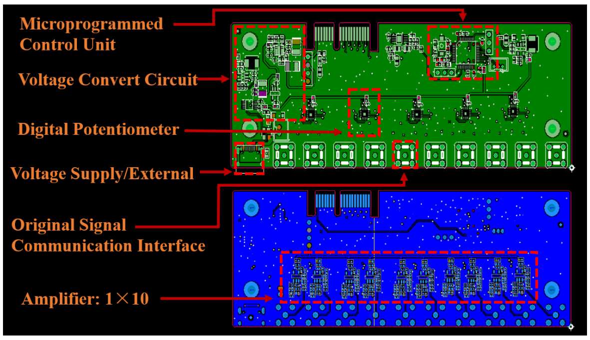

Fig. 4. Amplifier board: composed of a front amplifier, SiPM bias voltage/temperature compensation circuit, digital potentiometer, voltage conversion circuit, and microprogrammed control unit (MCU).

acquisition system (DAQBOX). The board is powered by a 5 V/2 A output power adapter with a c-type USB interface. The gain is also adjusted via a USB connection to the computer. The voltage converter can convert the external input 5 V voltage into the bias voltage needed by the SiPM, the power supply to the MCU and the positive/negative voltage needed by the front amplifier.

3.3. Field of view

Since the PPGID is made up of many pixelated detectors, like the eye of a fly, the field of view (FOV) that each eye can capture plays a basic role. There are three steps to determine the FOV of a PPGID. 1) FOV model for single pixel: in this step the geometric mathematical model determines how large a field of view each eye can see. 2) Multi-FOV along the beam direction: this step determines how faraway a field of view the PPGID can see the target clearly along the beam direction. 3) Multi-FOV in the vertical direction: this step determines how faraway a field of view the PPGID can see the target clearly in the vertical direction. 2) and 3) help us to put PPGID at a right place for a specific application.

Table 1. FOV parameters of PPGID in beam direction and vertical direction.

Parameter	Value for prototype	Unit	Explanation	Impact to FOV	Direction
a	0.5	cm	Cross width of the scintillator	+	Beam direction
d	15	cm	Distance to target	+	
H	8	cm	Length of grating shielding	-	
A	1	cm	Outside width of grating	+	Vertical direction
θ	4	degree	Angle between modules	+	

The field of view (FOV) is determined by the geometric parameters of the PPGID. For a single module, the FOV is controlled by the geometric parameters a, d, and H. Considering multiple modules in the vertical direction, the FOV is also controlled by A and θ. These parameters are summarized in Table 1 and the second column is the recommended value for the prototype, as shown in figure 5, 6, 7. The impact on the FOV marked with + means that the parameter and FOV are positively correlated and that marked with - means that the parameter and FOV are negatively correlated.

3.3.1. *FOV for a single pixel*

Every pixel of this detector has an independent field of view that is determined by the geometry of the grating hole, as shown in Figure 5. The blue block stands for the target phantom where gamma ray will be generated when proton

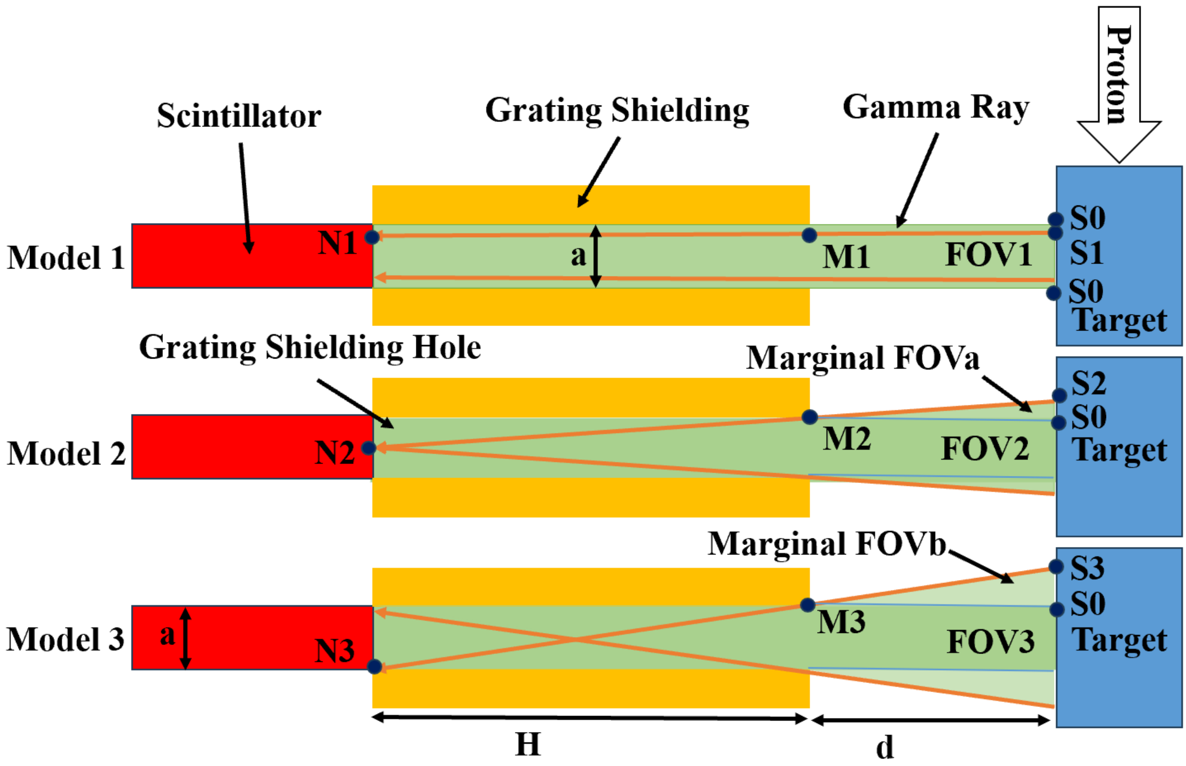

Fig. 5. Field of view for every pixel in three cases. The blue block is the target phantom where gamma ray will be generated when proton irradiate. S0∼S3 are special gamma source points in each model. The yellow blocks are grating shielding (collimator) and green areas are possible paths of the gamma ray from target to scintillators. The orange lines are special gamma rays and M1∼M3 are points on the corner of the collimator. The red block is scintillator and N1∼N3 are special points in each model the gamma rays reach the surface of scintillator.

irradiate. S0∼S3 are special gamma source points in each model. The yellow blocks are grating shielding (collimator) and green areas are possible paths of the gamma ray from target to scintillators. The orange lines are special gamma rays and M1∼M3 are points on the corner of the collimator. The red block is scintillator and N1∼N3 are special points in each model the gamma rays reach the surface of scintillator. The geometric parameters *a,d,*and *H* are defined in table 1.

There are three mathematical models for single pixel FOV calculation. The ideal case is shown in Figure 5 Model 1, all the gamma rays enter the grating shielding hole in parallel, and the scintillator views the target only of the same cross size of the crystal. Specifically, the calculation for FOV1, is shown in Equation 1.

$$FOV1 = (S0 - S0')^2 = a^2 \tag{1}$$

The second mathematical model is shown in figure 5 Model 2, the gamma ray from S2 can pass through M2 at the grating corner and reach the centre of the scintillator N2, where the gamma ray has a high probability of forming a full energy peak (FEP). In this model, there is a marginal , as shown in Equation 2. FOV2 is the summary of FOV1 and the marginal FOV$_a$.

$$\begin{cases} FOV_a = 4*(S2-S0)*a = 2\dfrac{d}{H}*a^2 \\ FOV2 = FOV1 + FOV_a = \left(1+2\dfrac{d}{H}\right)a^2 \end{cases} \tag{2}$$

In the third model as shown in figure 5 Model 3, the gamma ray from S3 can just pass through M3 and reach the corner of scintillator N3, where the gamma ray has a low probability of forming an FEP. In this case, there is a larger marginal FOV_b, as shown in Equation (3). FOV3 is the summary of FOV1 and the marginal FOV_b .

$$\begin{cases} FOV_b = 4*(S3-S0)*a = 4\dfrac{d}{H}*a^2 \\ FOV3 = FOV1 + FOV_b = \left(1+4\dfrac{d}{H}\right)a^2 \end{cases} \tag{3}$$

Regardless of which model is used, lower a and d values and a larger H value can be used to obtain a lower FOV. After all the components are manufactured, a and H are fixed. The distance to the target d is the only adjustable parameter that can control the FOV in the experimental test.

The FOV calculations for different cases at different distances are shown in Table 2. Ideally FOV1 will not change with the distance between the target and the PPGID. FOV2 and FOV3 increase with distance, and FOV3 is much larger

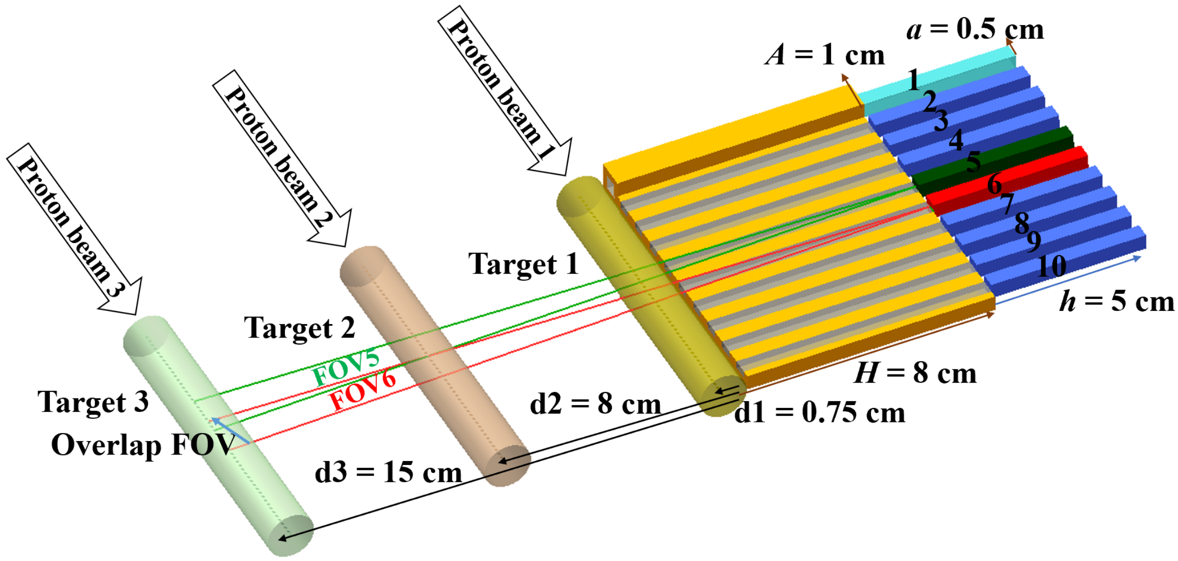

Fig. 6. Field of view along the beam direction. There is an overlap FOV region when the target distance is larger than 8 cm, for example, overlap of FOV5 and FOV6. If the distance is smaller than 8cm, the FOVs of each pixel are independent of each other.

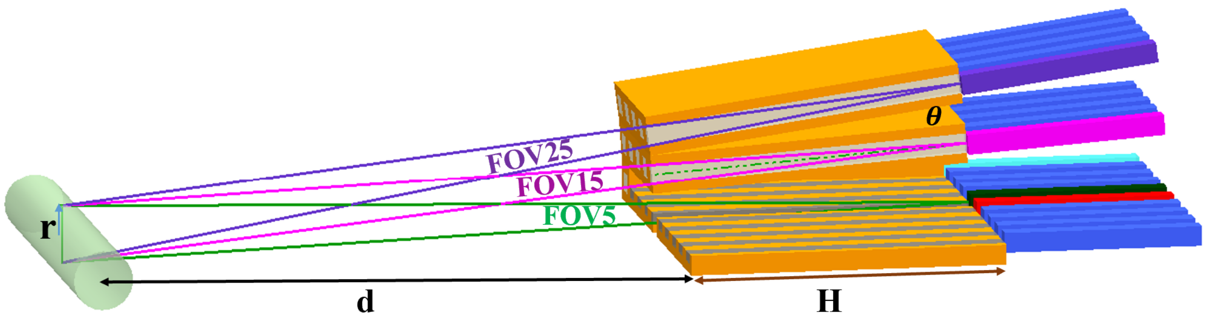

Fig. 7. Field of view in the vertical direction. *A* certain angle θ is formed between the modules to ensure that the pixels from different modules view the same central position.

Table 2. FOV calculations for different cases at different distances.

Distance / FOV(cm^2)	d0	d1	d2	d3
	0cm	0.75cm	8cm	15cm
FOV1	0.25	0.25	0.25	0.25
FOV2	**0.25**	**0.30**	**0.75**	**1.19**
FOV3	0.25	0.34	1.25	2.13

than FOV2. However, FOV3 has a low probability of forming FEP. In this study, FOV2 is used as a compromise in the following discussion, as determined by geometric parameters a , d and H.

3.3.2. *Multi-FOV along the beam direction*

Every module has 10 pixels, and their multiple FOVs are important for future range measurement. A multifield of view along the beam direction is shown in figure 6. Better independence of the FOV is obtained. When the PPGID is closer to the target, there is an overlap FOV region when the target distance is larger than 8 cm. If the distance is smaller than 8 cm, the FOVs of each pixel are independent of each other.

The FOV angle is determined by Equation 4. This angle has nothing to do with the distance between the target and detector. This angle is only controlled by the detector parameters cross width a and grating lengrh H. For a given detector size, increasing the grating length can narrow this angle. This will increase the independence for each pixel.

$$\varphi = 2 * \tan^{-1}\left(\frac{a/2}{H}\right) = 2 * \tan^{-1}\left(\frac{0.5cm/2}{8cm}\right) = 3.58^{\circ} \tag{4}$$

Thus, the distance resolution of every pixel along the beam direction is shown in Equation 5 :

$$l = \varphi * (d + H) \tag{5}$$

If d = 15 cm, then l = 1.44 cm. If d = 8 cm, then l = 1 cm .

If d = 0 cm, then l = 0.5 cm .

3.3.3. Multi-FOV in the vertical direction

A multifield of view in the vertical direction is shown in figure 7. A certain angle θ is formed between the modules to satisfy Equation 6 to ensure that the pixels from different modules view the same central position.

$$\theta = 2 * \tan^{-1}\left(\frac{A/2}{d}\right) \tag{6}$$

Letting $\theta = \phi$, we have d = 16.13 cm . At this distance, all modules will view the same place in the vertical direction in a field of r = 0.75 cm as calculated by Equation 7.

$$r = \theta * (d + H)/2 \tag{7}$$

If the target approaches the detector, the 3 modules will view different places in the vertical direction. Then, they will be independent of each other, similar to the beam direction. If the angle is $\theta = 0$, then no difference is observed in the beam direction configurations.

3.3.4. DAQBOX

The data acquisition system (DAQBOX-32-125M) is a standard module. The module has 32 channels (Lemo) and 1∼30 are engaged by the 30 amplified signals from the front-end electronics. The ADC dynamic range is -2 V to 2 V. The Sampling rate is 125 M. The maximum data throughput is 100 Mbyte/s in TXT format with gigabit network port. The maximum count rate for every independent channel is 10^6 count/s. Its dead time is 1 microsecond and the temporal resolution is 8 ns.

4. VERIFICATION WITH RADIOACTIVE SOURCES

A Series of tests are conducted with different radioactive sources. The radioactive sources ^{22}Na and ^{232}Th (activity of 6E5 Bq) are used to test the performance of the PPGID prototype. The major characteristic gamma rays are summarized in table 3 . The ^{232}Th gamma spectrum has many peaks spanning out to 2.6 MeV from its daughter isotopes. The 1460 keV gamma ray is easily detected from ^{40}K in the background when no shielding is present around the detector. Note that the energy range in the following tests are limited by the highest gamma ray 2.6 MeV. However, this is not the end of BGO and experiments results proved that its dynamic range up to 8 MeV[15][49].

4.1. Data acquisition software

All needed functions from Section 2 are achieved by our dedicated data acquisition software, as shown in figure 8, Its major functions include acquisition, count histograms, and brightness. The software can acquire gamma spectrum data for every pixel shown on the same screen when irradiation starts. Energy calibration and energy windows can be conducted using the buttons in the right column. The software can directly generate count histograms and highlight plots, as shown in figure 14 and 15, these can be directly used to determine the position of the gamma source and the distal fall off of the Bragg peak in future tests. The default mode is online measurement. The offline mode can also be used to analyse previous experimental data.

Table 3. Characteristics of sodium-22 and thorium-232

Source	Gamma ray [keV]	Gamma emission probability
^{22}Na	511	179.8%
	1274	99.9%
^{232}Th	238 (212Pb)	43.30%
	338 (228Ac)	11.27%
	583 (208Ti)	84.50%
	911 (228Ac)	25.80%
	969 (228Ac)	15.80%
	2614 (208Ti)	99%
^{40}K	1460	10.70%

4.2. Energy calibration and spectra measurements

To test the energy response for every pixel, compound sources ^{22}Na and ^{232}Th are placed at different locations ① to ⑥ around the PPGID, as shown in figure 9. b) The origin of the coordinate system is defined at the centre of pixel 11 as show in figure 9 a). The ^{232}Th source was thorium anhydride (ThO_2) inside a glass bottle. ^{22}Na is placed behind ^{232}Th, figure 9 a). A shielding grating is not used in this case to increase the detection efficiency, take into account the effect of noise, we added the threshold for the signal, the threshold is 20 lsb (lsb, least significant bit , 1 lsb about equal 1 mV) in this test.

The gamma spectra of ^{22}Na and ^{232}Th detected by $LaBr_3$ modules 1 (CH1-10) and 2 (CH11-20) are shown in figure 10. The left panel is before energy calibration, and the right panel is after energy calibration. Details of the energy calibration method have already been presented in our previous work in Section 3.2[45]. For $LaBr_3$, three characteristic gamma rays were selected to calibrate the spectra: 238, 511 and 1460 keV. The uncalibrated spectra show maxima at different channels, and the calibrated spectra show the same distinct gamma rays for every pixel as in Table 3. Since $LaBr_3$ has high energy resolution, low-energy peaks close to each other are also identified, these include the peaks at 511 and 583 keV and those at 911 and 969 keV. High-resolution gamma ray measurements are the basis for element determination based on PGSRA.

The gamma spectra of ^{22}Na and ^{232}Th detected by BGO module 3 (CH21-30) are shown in figure 11. The left panel is before energy calibration, and the right panel is after energy calibration. For BGO, three characteristic gamma rays are selected to calibrate the spectra: 1274 , 1460 and 2614 keV.

Fig. 8. Data acquisition software for the PPGID. Its major functions include acquisition, count histograms, and brightness. Energy calibration and energy windows can be conducted using the buttons in the right column.

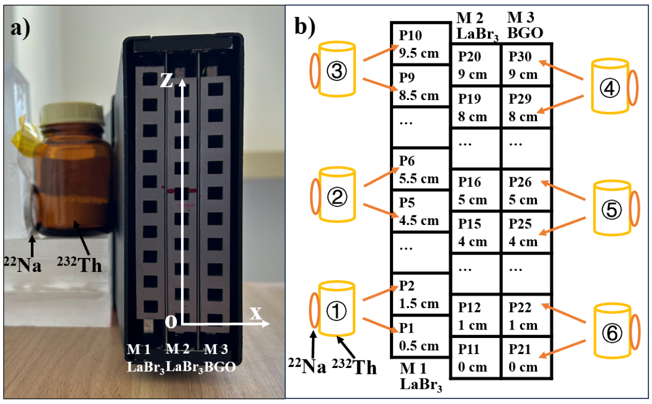

Fig. 9. Energy response test set up with compound ^{22}Na and ^{232}Th are placed at different locations ① to ⑥ around the PPGID. The left picture is a physical picture, and the right picture is a schematic.

The uncalibrated spectra show maxima at different channels, and the calibrated spectra show distinct gamma rays for every pixel as in Table 3. Since the energy resolution of BGO is not as good as that of $LaBr_3$, the low-energy peaks are not distinct at energies lower than 1000 keV.

Thus, the energy response of $LaBr_3$ modules is at least 0.03∼2.6 MeV and has high energy accuracy in low-energy gamma ray detection which can distinguish between 511/583 keV and 911/969 keV. The energy response of the BGO module is at least 1∼2.6 MeV and has high efficiency in high-energy gamma ray detection. Moreover, the energy resolution of $LaBr_3$ is good for low energy, and the efficiency of BGO is high for high energy.

4.3. FOV and source positions

To verify the different FOV impacts for gamma ray detection, radioactive source ^{22}Na was placed at five distances away from the PPGID: 0 , 5 , 10 , 15 , and 20 cm, as shown in figure 12. ^{22}Na is attached to an acrylic plate, and the centre of the radioactive source is aligned with P16 where z = 5 cm. From left to right are module 1 $LaBr_3$, module 2 $LaBr_3$, and module 3 BGO. The irradiation times is 155 , 350 , 300 , 320 and 420 s for each distance. $LaBr_3$ module 1 and module 2 are misaligned by 0.5 cm in this section as only same types of crystal get similar spectrum as shown in section 4.2.

In the software one can set any energy window to determine the source position as shown in figure 13. The first two windows are set around the characteristic gamma rays, and the others are set by arbitrarily selecting wide continuous energy intervals.

The performance of energy window [0, 300] keV is poor beacuse of its high noise level. Thus, we define the Signal to Noise Ratio (SNR) in our case to choose the proper energy window: SNR = peak count/average noise count. The SNRs from the [450, 600] keV and [1200, 1450] keV Energy window at characteristic gamma rays from ^{22}Na are much better than those of the others. The SNR of the BGO module is better than that of $LaBr_3$ module. Thus, in this study energy windows were set to 450 to 600 keV for the 511 keV gamma ray and 1200 to 1450 keV for the 1274 keV gamma ray.

The peak at 511 keV is the characteristic gamma ray from ^{22}Na. Thus, the first energy window is set as 450 keV to 600 keV. The gamma counts of each pixel are automatically recorded and formed into histograms and highlight plots, as shown in figure 14. M1 and M2 with $LaBr_3$ can measure the source position at P16, while M3 with BGO can measure the source position at P26.

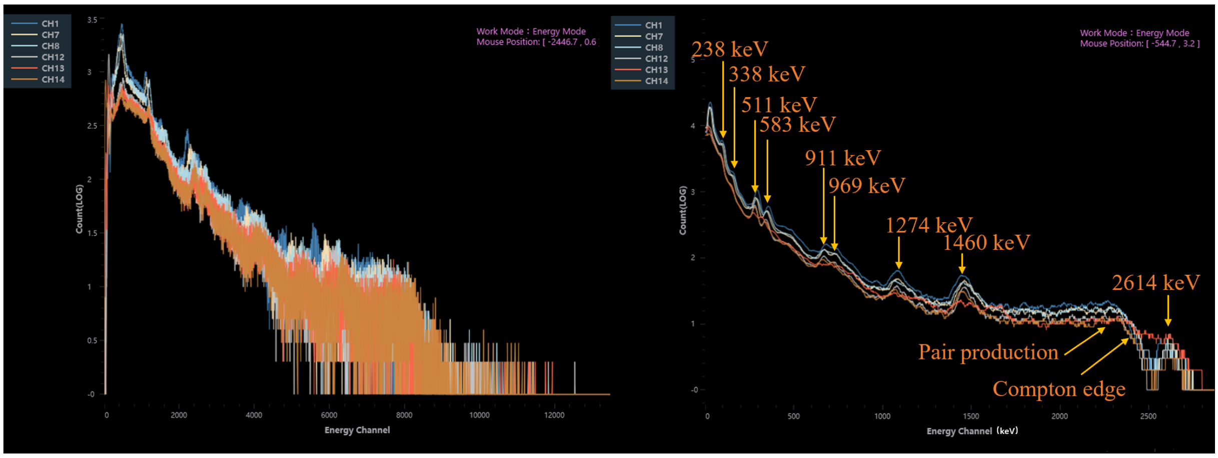

Fig. 10. Gamma spectra of ^{22}Na and ^{232}Th detected by the $LaBr_3$ module 1 (CH1, CH7, CH8) and module2 (CH12, CH13, CH14). Left: Before energy calibration. Right: After energy calibration.

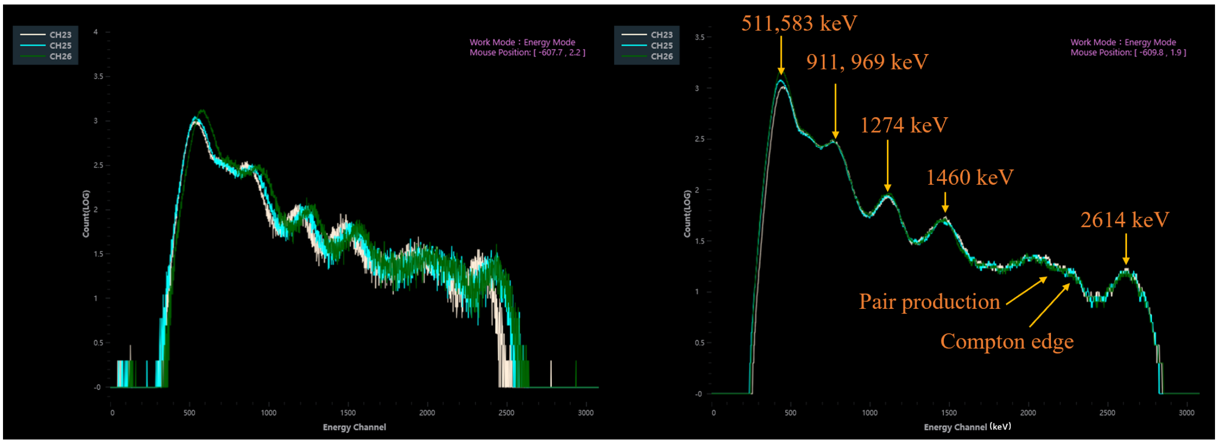

Fig. 11. Gamma spectra of ^{22}Na and ^{232}Th detected by BGO module 3 (CH23, CH25, CH26). Left: Before energy calibration. Right: After energy calibration

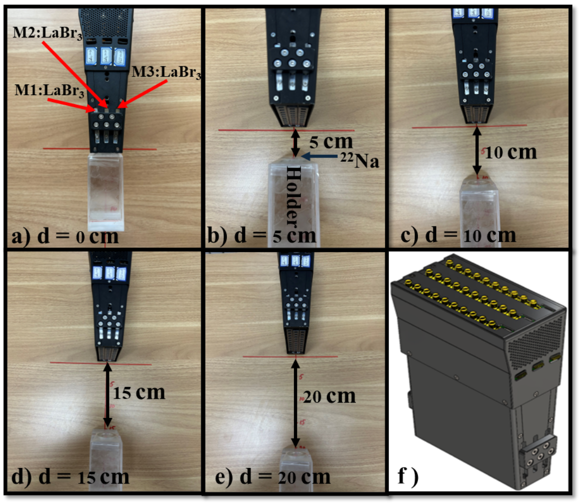

Fig. 12. Radioactive source ^{22}Na at different distances from the PPGID a) d = 0 cm to e) d = 20 cm. The source 22Na is on the front of holder, and prototype is shown in f)

In the beam direction, when the distance is smaller than 8 cm, only P16 in M2 is able to view the source. The counts of P15 and P17 rapidly increase when the distance increases to 15 and 20 cm, respectively. This is consistent with the mathematical analysis in Section 3.3.2. When the distance is less than 8 cm, the FOVs of each pixel are independent of each other. A small overlap FOV region is observed when the distance is 10 cm and a larger overlap FOV is observed at 15 cm and 20 cm. Thus, P5 and P6 in M1, P15 to P17 in M2, and P25 to P27 in M3 are highlighted.

In the vertical direction, M1 and M3 cannot view the source when the distance is less than 10 cm. P5 to P6 in M1 and P26 in M3 can view the source when the distance increases to 10 cm, as shown in Figure 14 c). This is consistent with the mathematical analysis in Section 3.3.3. At a distance 15 cm in Figure 14 d), all modules will view the same place in the vertical direction in a field of r = 0.75 cm, as calculated by Equation (7). The counts of P25 and P27 in M3 increase rapidly when the distance increases from 10 to 20 cm.

Thus, 15 cm is the recommended distance for future in-

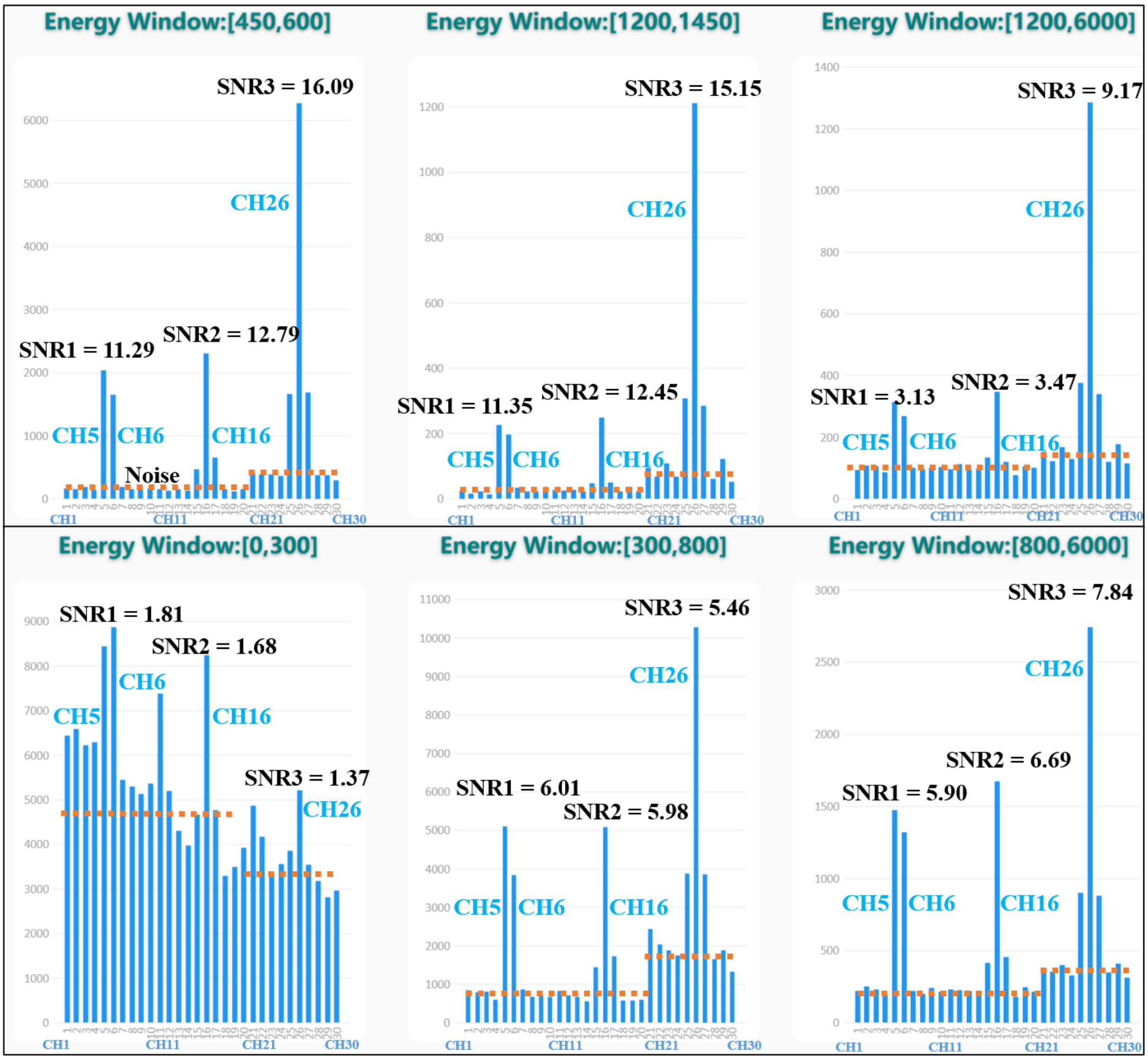

Fig. 13. Gamma count histograms from different energy windows at distance 15 cm. In each energy window, the horizontal axis is the pixel channel from module 1 to module 3, the vertical axis is the gamma count

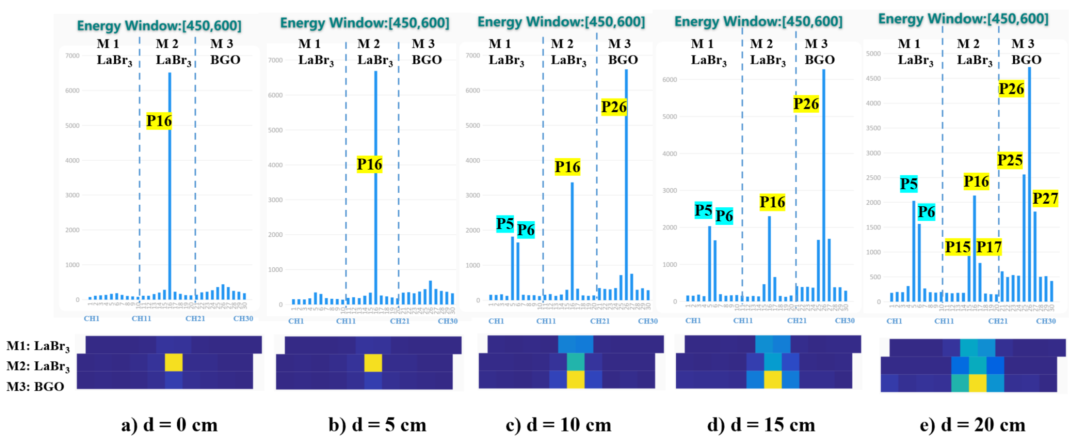

Fig. 14. Histograms and highlighted plots from the low-energy window [450, 600] keV. The above pictures are the histograms of each module at different distance and the below ones are the highlighted plots shows the measured position of the source.

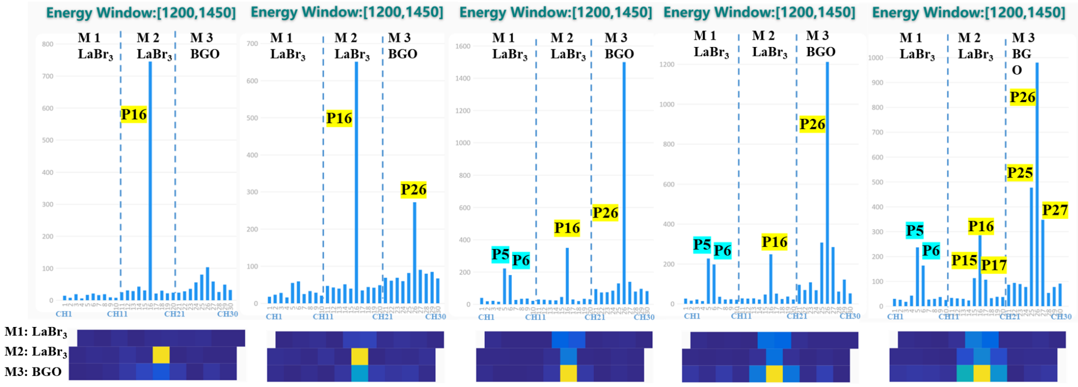

a) d = 0 cm b) d = 5 cm c) d = 10 cm d) d = 15 cm e) d = 20 cm

Fig. 15. Histograms and highlighted plots from the high energy window [1200, 1450] keV. The above pictures are the histograms of each module at different distance and the below ones are the highlighted plots shows the measured position of the source.

beam tests for proton range measurements to ensure the independence of each pixel, and M1 can work with M2 to increase the resolution as they are same type. BGO module has a much higher gamma count than $LaBr_3$ when the source enters the FOV of M3 at distances of 10 to 20 cm figure 14 c) to e). This is because BGO has a higher detection efficiency. The gamma count ratio of P26 to P16 is 2.7 in figure 14 c).

The peak at 1274 keV is the characteristic gamma ray from ^{22}Na. Thus, the second energy window is set to 1200 keV to 1450 keV. The gamma counts of each pixel are recorded and formed into histograms and highlight plots, as shown in figure 15. P16 and P26 show highlights at the correct places, which point to the gamma source. This is consistent with the results from the low-energy window, as shown in Figure 14. A larger distance has a wider FOV in the beam direction, and more than one pixel is able to view the source in all modules M1, M2, and M3.

M3 shows a better performance with a high energy window [1200, 1450] keV than with a low energy window [450, 600] keV. This is because the energy response of the BGO module is 1∼2.6 MeV and the efficiency of BGO is high for a high energy window. For example, in Figure 15 d) where the distance is 15 cm, the gamma count from P16 in M2 $LaBr_3$ is 249, while that from P26 in M3 BGO is 1212. The efficiency ratio between BGO and $LaBr_3$ is ∼4.8 for a high energy window [1200, 1450] keV, while it's only 2.7 for low energy window [450, 600]keV.

Thus, $LaBr_3$ and BGO can be complementary, the energy resolution of $LaBr_3$ is good for low energy, and the efficiency of BGO is high for high energy. In the clinic, 0.09 photons are generated by every proton [50]. There are approximately 1E9 to 1E10 protons for a single spot. Thus, 1E8 to 1E9 photons are generated per spot. The activity of the source is 6E5 Bq, and the irradiation time is 300 seconds. Thus, there are 1.8E8 photons in the previous tests, which is within the clinical range. Thus, a compound advanced imaging device, PPGID, based on the energy spectrum shows potential for application in particle therapy.

4.4. Misalignment fitting

The misalignment of the two modules can increase the position resolution as described in Section 3.1. In that case there are 20 pixels from M1 and M2. The data from the 20 pixels can be further used to accurately fit the source position in figure 16. Gaussian fitting of both windows showed that the centre position of the radioactive source was 4.96 cm. Thus, the misalignment of several modules is a powerful tool in radioactive sources' position measurements.

There is a gap between radioactive sources' position measurements and proton range measurements. radioactive source is a point gamma ray while proton beam in tissue will generate a line gamma ray which consists with many points. For pencil beam scanning mode in proton therapy, PPGID has the potential to detect the distal fall-off location and thus measure the proton range by reproduce the hundreds of gamma sources.

5. CONCLUSIONS

The first prototype of a pixelated prompt gamma imaging detector system (PPGID) including three modules is designed, manufactured, and tested with radioactive sources in this work. To fulfil the requirements intended for future proton therapy applications, dedicated design, software, and methods are used in this prototype development.

1)The detector should be pixelated to obtain gamma ray photons along the beam path. To achieve longitudinal spatial resolution, only photons perpendicular to the beam direction are allowed to enter the detector crystal.

Solutions:

I) The FOVs of single pixels and multiple modules are analysed mathematically based on the geometric parameters *a, d, H* and *A* and θ. PPGID can correctly measure the source position, and 15 cm is the recommended distance for future in-beam tests for proton range measurements to ensure the independence of each pixel. At this distance, multiple mod-

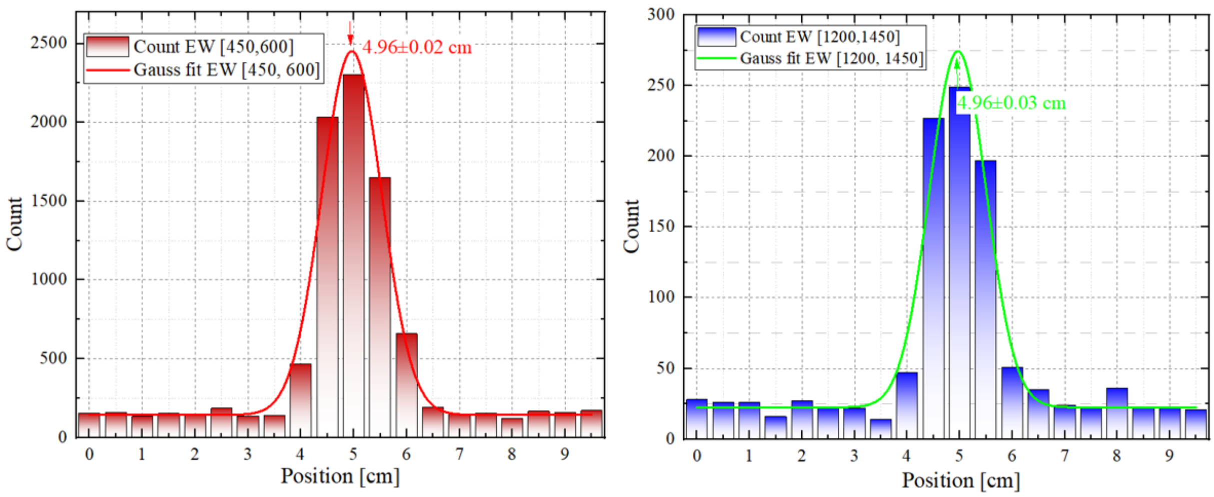

Fig. 16. Position measured by Gaussian fitting gamma distribution of energy windows [450, 600] keV and [1200, 1450] keV. The red is the energy windows [450,600] keV, the blue is the energy windows [1200,1450] keV. The measured source position is 4.96 cm for both.

ules misaligned in the vertical direction can work with each other to increase the radioactive sources' position measurement resolution. But this method is valid only for same type modules such as M1 and M2 made of $LaBr_3$ both.

II) Grating shielding with a 0.5 cm× 0.5 cm hole is designed and manufactured(the material of the collimator is tantalum, and its length is 8 cm, lateral thickness is 0.5 mm). The function of the grating is to filter the photons so that only gamma rays parallel to the grating enter the scintillator. This feature ensures that the PPGID has the potential to detect the distal fall-off location and thus measure the proton range.

2)The gamma ray energy spectral response of the detector should be as wide as possible, and the energy resolution should be high. The ideal energy response range is 0.03∼8 MeV.

Solutions:

Compound modules are used in PPGID. $LaBr_3$ and BGO can be complementary, the energy resolution of $LaBr_3$ is good for low energy, and the efficiency of BGO is high for high energy. The tested energy response of $LaBr_3$ is 0.03∼2.6 MeV, and that of BGO is 1∼2.6 MeV. Low energy peaks close to each other can be distinguished by $LaBr_3$, such as at 511 and 583 keV and at 911 and 969 keV. Note that the energy range in the following tests are limited by the highest gamma ray 2.6 MeV. However, this is not the end of BGO and experiments results proved that its dynamic range up to 8 MeV.

3)To retrieve tissue elements as needed by PGSRA, every pixel should independently measure the gamma spectrum. Thus, the energy scale should be determined during gamma detection or before data analysis.

Solutions:

I) Specific front-end electronics for every independent pixel are developed for the PPGID system; this ensures that the parameters, such as voltage and gain, can be adjusted pixel by pixel. The original SiPM signal is independently amplified by the forwards amplifier circuit and then output to the back-end data acquisition system. The software can manage the gamma spectrum for every pixel. II) The energy calibration method is adopted for every pixel. The uncalibrated spectra peak at different channels, and the calibrated spectra show the same distinct gamma rays for every pixel. This method ensures energy consistency.

4)Different energy windows can be set in the energy spectrum to facilitate data analysis. Solutions: Any energy window could be set up in the data acquisition and analysis software. In the tests, a low energy window [450, 600] keV and a high energy window [1200, 1450] keV are selected since ^{22}Na has characteristic gamma rays of 511 and 1274 keV.

The comparison with existing gamma detectors and PPGID is shown in Table 4. The difference is that the PPGID is expected to measure a 2-dimensional map as it can generate the highlighted plots at each pixel. While the proton range estimation performance needs to be verified by more in-beam experiments in the future. Thus, $LaBr_3$ and BGO can function together due to their complementary nature. A compound advanced imaging device, PPGID, based on the energy spectrum shows great potential for application in particle therapy.

The next step we will verify its performance in range assesment on the cyclotron of CIAE (China institute of atomic energy) and plan to use the proton energy of 68, 78, 88 MeV irradiate on the water and PMMA phantom. The in-beam test results will be presented in our next manuscript.

6. ACKNOWLEDGMENT

This work was supported by the National Natural Science Foundation of China (U1932209, 11975315, U22167202, U2167201). The authors kindly acknowledge the great support from engineers Wei Hu and Ze-Wei Shi.

Table 4. FOV calculations for different cases at different distances.

Item \ Detector	Knife-edge slits (KES[40])	Multiparallel slits (MPS[41])	Pixelated system in this work (PPGID)
Collimator	Single slit	Multi slits	Pixelated slits
Measuring position	Relative location	Absolute location	Absolute location
Measurement fields	1 dimension	1 dimension	2 dimensions
Range estimation precision	About 2 mm	Less than 1 mm	radioactive source position$\sim$ 0.3 mm
Spectroscopy measurement	yes	yes	Specifically, yes

7. REFERENCE

[1] H. Paganetti, C. Beltran, S. Both, *et al.*, Roadmap: proton therapy physics and biology. Phys Med Biol. **5**, 66(2021). doi:10.1088/1361-6560/abcd16

[2] R.I. MacKay. Image guidance for proton therapy. Clin Oncol. **293–298** 5 30 (2018). doi:10.1016/j.clon.2018.02.004

[3] J.G. Park, C.H. Min. Development of an array-type prompt gamma detection system for the online measurement of the range of the proton beam in a patient: a Monte Carlo feasibility study. J Korean Phys Soc. **888–891** 3 52 (2008). doi:/10.1007/s41605-017-0032-0

[4] H.Paganetti. Range uncertainties in proton therapy and the role of Monte Carlo simulations. Phys Med Biol. **R99** 11 57 (2012). doi:/10.1088/0031-9155/57/11/R99

[5] Y. Han, X.B. Tang, C.G. Geng, *et al.*, Investigation of in vivo beam range verification in carbon ion therapy using the Doppler Shift Effect of prompt gamma: A Monte Carlo simulation study. Radiat Phys Chem. **72–81** 162 (2019). doi:/10.1016/j.radphyschem.2019.04.036

[6] B. Kopp, S. Meyer, A. Mairani, *et al.*, Roadmap: helium ion therapy. Phys Med Biol. **15TR02** 162 (2022). doi:/10.1088/1361-6560/ac65d3

[7] R. Dal Bello, P. Magalhaes Martins, J. Graca, *et al.*, Results from the experimental evaluation of $CeBr_3$ scintillators for ^{4}He prompt gamma spectroscopy. Med Phys. **3615–3626** 8 46 (2019). doi:/10.1002/mp.13594

[8] G. Battistoni, F. Collamati, L.E. De, *et al.*, Design of a tracking device for on-line dose monitoring in hadrontherapy. Phys Res Sect A. **679-683** 845(2017). doi:/10.1016/j.nima.2016.05.095

[9] K. Parodi, F. Pönisch, W. Enghardt, *et al.*, The feasibility of in-beam PET for accurate monitoring of proton therapy: Results of a comprehensive experimental. IEEE, Nucl Sci Symp Conf Rec. **2160-2164** 162 (2004). doi:/10.1109/nssmic.2004.1462690

[10] F. Pennazio, V. Ferrero, G. D.Onghia, *et al.*, Proton therapy monitoring: Spatiotemporal emission reconstruction with prompt gamma timing and implementation with PET detector. Phys Med Biol. **6** 67 (2022). doi:/10.1088/1361-6560/ac5765

[11] K. Parodi, PET monitoring of hadrontherapy. Nucl Med Rev. **37-42** 15 (2012). doi:/10.1088/1361-6560/ac65d3

[12] M.G. Bisogni, A. Attili, G. Battistoni, *et al.*, INSIDE in-beam positron emission tomography system for particle range monitoring in hadrontherapy. J Med Imaging. **011005** 162 (2016). doi:/10.1117/1.jmi.4.1.011005

[13] Z.X He, L.K. Hou, R. Sun, *et al.*, The INSIDE project: In-beam PET scanner system features and characterization. J Instrum. **3** 12 (2017). doi:/10.1088/1748-0221/12/03/C03051

[14] S. Aldawood, P.G. Thirolf, A. Miani, *et al.*, Development of a Compton camera for prompt-gamma medical imaging. Radiat Phys Chem. **190-197** 29 (2017). doi:/10.1016/j.radphyschem.2017.01.024

[15] F. Hueso-Gonzalez, G. and Pausch, J. Petzoldt, *et al.*, Prompt Gamma Rays Detected With a BGO Block Compton Camera Reveal Range Deviations of Therapeutic Proton B. IEEE Trans Radiat Plasma Med Sci, **76-86** 1 (2016). doi:/10.1109/tns.2016.2622162

[16] A. Kishimoto, J. Kataoka, T. Nishiyama, *et al.*, Demonstration of three-dimensional imaging based on handheld Compton camera. J Instrum. **11** 10 (2015). doi:/10.1088/1748-0221/10/11/P11001

[17] J.C. Polf, S. very, D.S. Mackin, *et al.*, Imaging of prompt gamma rays emitted during delivery of clinical proton beams with a Compton camera: Feasibility studies for range verification. Phys Med Biol. **7085-7099** 60 (2015). doi:/10.1088/0031-9155/60/18/7085

[18] J.P. Zhang, X. Xiao, and B. Zhang,*et al.*, A Portable Three-Layer Compton Camera for Wide-Energy-Range Gamma-ray Imaging: Design, Simulation and Preliminary Testing. SENSORS. 23(21), 8951. doi:10.3390/s23218951

[19] Y.L. Chen, H.K. Wang and S.Y. Zhang,*et al.*, Hi'CT: a pixel sensor-based device for ion tomography. NUCL SCI TECH. **2210-3174** 60 (2023). doi:10.1007/s41365-023-01251-x

[20] S.Y. Zhang, Z.X Wang and H.B. Yang,*et al.*, Hformer: highly efficient vision transformer for low-dose CT denoising. NUCL SCI TECH. **2210-3174** 60 (2023). doi:/10.1007/s41365-023-01208-0

[21] M.P. Magalhaes, B.R. Dal, B. Ackermann, *et al.*, PIBS: Proton and ion beam spectroscopy for in vivo measurements of oxygen, carbon, and calcium concentra. Sci Repl. **1–14** 10 (2020). doi:/10.1038/s41598-020-63215-0

[22] J.L. Wang, X.G. Wu, Z.F. Li, *et al.*, Prompt gamma spectroscopy retrieval algorithm for element and density measurements accelerated by cloud computing. Aip Conf Proc. **1097** 10 (2022). doi:10.3389/fphy.2022.961162

[23] F. Hueso-González, M. Rabe, T.A. Ruggieri, *et al.*, A full-scale clinical prototype for proton range verification using prompt gamma-ray spectroscopy. Phys Med Biol. **18** 63 (2018). doi:/10.1088/1361-6560/aad513

[24] J.H. Park, S.H. Kim, Y.M. Ku, *et al.*, Multi-slit prompt-gamma camera for locating of distal dose falloff in proton therapy. Nucl Eng Technol. **1406–1416** 51 (2019). doi:/10.1016/j.net.2019.03.008

[25] J.L. Wang, L. Cruz, M. Lu, *et al.*, Pixelated prompt gamma imaging detector for online measurement of proton beam: Monte Carlo feasibility study by FLUKA. Radiat Detet Technol and Methods. **2** 162 (2022). doi:/10.1007/s41605-017-0032-0

[26] H.Y. Zhang, P. Fan, S. Wang, *et al.*, Design and performance evaluation of a BGO+ SiPM detector for high-energy prompt gamma imaging in proton therapy monitoring. IEEE Trans Radiat and Plasma Med Sci. **184–193** 162 (2020). doi:/10.1109/trpms.2020.2972594

[27] R.K. Parajuli, M. Sakai, R. Parajuli, *et al.*, Development and Applications of Compton Camera—A Review. Sensors. **19** 22 (2022). doi:/10.3390/s22197374

[28] E. Munoz, A. Ros, M. Borja-Lloret, *et al.*, Proton range verification with MACACO II Compton camera enhanced by a neural network for event selection. Sci Rep. **1-12** 1(2021). doi:/10.1038/s41598-021-88812-5

[29] C. Richter, G. Pausch, S. Barczyk, *et al.*, First clinical application of a prompt gamma based in vivo proton range verification system. Rad Oncol. **232–237**2(2016). doi:/10.1016/j.radonc.2016.01.004

[30] I. Perali, A. Celani, L. Bombelli, *et al.*, Prompt gamma imaging of proton pencil beams at clinical dose rate. Phys Med Biol. **5849-5871** 19 (2014). doi:/10.1088/0031-9155/59/19/5849

[31] H.Y. Zhang, P. Fan, Peng and T.P Xu, *et al.*, Scintillation Detector Design Study for Prompt Gamma Photon Detection in Proton Therapy Monitoring. IEEE Nucl Sci Symp Med Imaging Conf NSS/MIC. **1-4** (2017). doi:/10.1109/NSSMIC.2017.8532768

[32] Y. Han, X.B. Tang and C.R. Geng, *et al.*, Investigation of in vivo beam range verification in carbon ion therapy using the Doppler Shift Effect of prompt gamma: A Monte Carlo simulation study. RADIAT PHYS CHEM. **72-81** (2019). doi:/10.1016/j.radphyschem.2019.04.036

[33] C.R. Geng, Y. Han and X.B. Tang, *et al.*, Evaluation of using the Doppler shift effect of prompt gamma for measuring the carbon ion range in vivo for heterogeneous phantoms. NUCL INSTRUM METH A.**0168-9002** (2020). doi:/10.1016/j.nima.2020.163439

[34] Y.J.Yu, P.Y. Qi and H.Peng. Feasibility study of 3D time-reversal reconstruction of proton-induced acoustic signals for dose verification in the head and the liver: A simulation study. MED PHYS.**0094-2405** (2021). doi:/10.1002/mp.15046. Epub

[35] A.C. Knopf, A. Lomax, *et al.*, In vivo proton range verification: A review. Phys Med Biol. **15** 58 (2013). IEEE Nucl Sci Symp Med Imaging Conf NSS/MIC. doi:/10.1088/0031-9155/58/15/R131

[36] J. Krimmer, D. Dauvergne, J.M. tang, *et al.*, Prompt-gamma monitoring in hadrontherapy: A review. Nucl Instruments Methods Phys Res Sect A Accel Spectrometers. **58–73**878 (2018). doi:/10.1016/j.nima.2017.07.063

[37] P. Fan, W.Z. Lu and H.Y. Zhang, *et al.*, TianyuDevelopment and Performance Evaluation of a Prompt Gamma Imaging System for Real-time Proton Therapy Monitoring. IEEE Nucl Sci Symp Med Imaging Conf NSS/MIC. **1-5** (2018). doi:10.1109/NSSMIC.2018.8824656

[38] W.Z. Lu, P. Fan and Y.Q. Liu, *et al.*, Characterization and Modeling of Knife-Edge Slit Collimator Response for MeV Prompt Gamma Photons in Proton Therapy Monitoring. IEEE Nucl Sci Symp Med Imaging Conf NSS/MIC. **1-4** (2017). doi:10.1109/NSSMIC.2017.8532777

[39] J.H. Park, S.H. Kim, Y. Ku, *et al.*, Comparison of knife-edge and multi-slit camera for proton beam range verification by Monte Carlo simulation. Nucl Eng Technol. **51**:533–538.(2019). doi:/10.1016/j.net.2018.10.002

[40] J. Smeets, F. Roellinghoff, G. Janssens , *et al.*, Experimental comparison of knife-edge and multi-parallel slit collimators for prompt gamma imaging of proton pencil beams. Front Oncol. **6**:1-8.(2022). doi:/10.3389/fonc.2016.00156

[41] Y.Ku, J.Cho, S.Cu, *et al.*, Tackling range uncertainty in proton therapy: Development and evaluation of a new multi-slit prompt-gamma camera (MSPGC) system. NUCL ENG TECHNOL. (2023). doi:10.1016/j.net.2023.05.028

[42] J.C. Polf, S. Peterson, G. Ciangaru, *et al.*, Prompt gamma-ray emission from biological tissues during proton irradiation: a preliminary study. Phys Med Biol. **731-743** 54 (2009). doi:/10.1088/0031-9155/54/3/017

[43] J.M. Verburg, H.A. Shih, J. Seco, *et al.*, Simulation of prompt gamma-ray emission during proton radiotherapy. Phys Med Biol. **5459-5472** 57 (2012). doi:/10.1088/0031-9155/57/17/5459

[44] J.C. Polf, R. Panthi, D.S. Mackin, *et al.*, Measurement of characteristic prompt gamma rays emitted from oxygen and carbon in tissue-equivalent samples during proton beam irradiation. Phys Med Biol. **17** 58 (2013). doi:/10.1088/0031-9155/58/17/5821

[45] J.L. Wang, X.G. Wu, Z.Y. He, *et al.*, Compact pixelated scintillator detector investigation for gamma ray detection. Eng Res Express. (2024). 10.1088/2631-8695/ad43b4

[46] G. Pausch, J. Berthold, W. Enghardt, *et al.*, Detection systems for range monitoring in proton therapy: Needs and challenges. Nucl Instruments Methods Phys Res Sect A Accel Spectrometers. **954** (2020). doi:/10.1016/j.nima.2018.09.062

[47] D. Zhang, P. Fan, W. Lu, *et al.*, Accurate Modeling of Multi Knife-edge Slit Collimator System Response for MeV Prompt Gamma Photons in Proton Therapy Monitoring. IEEE Nucl Sci Symp Med Imaging Conf NSS/MIC. **1–4** 162 (2018). doi:/10.1109/NSSMIC.2018.8824338

[48] W. Lu, P. Fan, H. Liu, *et al.*, Prompt gamma imaging with a multi-knife-edge slit collimator for large FOV monitoring of scanned proton pencil beams. IEEE Nucl Sci Symp Med Imaging Conf Room-Temperature Semicond Detect Work NSS/MIC/RTSD. (2017). doi:/10.1109/NSSMIC.2016.8069396 Journal of Instrumentation

[49] F.Hueso, A.K.Biegun , P.Dendooven, *et al.*, Comparison of LSO and BGO block detectors for prompt gamma imaging in ion beam therapy. J INSTRUM. (2015). doi:10.1088/1748-0221/10/09/P09015

[50] J. Smeets, F. Roellinghoff, D. Prieels *et al.*, Prompt gamma imaging with a slit camera for real-time range control in proton therapy. Phys Med Biol. **57**:3371-3405. (2012). doi:/10.1088/0031-9155/57/11/337